Direct detection of plasticity onset through total-strain profile evolution

Stefanos Papanikolaou[1] and Mikko J. Alava[1,2]

[1]*NOMATEN Centre of Excellence, National Centre of Nuclear Research, A. Soltana 7, 05-400 Otwock-Świerk, Poland*
[2]*Department of Applied Physics, Aalto University, P.O. Box 11100, FI-00076 Aalto, Espoo, Finland*

Plasticity in solids is dependent on microstructural history, temperature, and loading rate, and sample-dependent knowledge of yield points in structural materials adds reliability to mechanical behavior. Yielding is commonly measured through controlled mechanical testing, in ways that either distinguish elastic (stress) from total deformation measurements or identify plastic slip contributions. In this paper, we show that yielding can be unraveled through statistical analysis of total-strain fluctuations during the evolution sequence of profiles, measured *in situ*, through digital image correlation. We demonstrate two distinct ways of quantifying yield locations in widely applicable crystal plasticity models for polycrystalline solids, using either principal component analysis or discrete wavelet transforms. We test and compare these approaches for synthetic data of polycrystals and a variety of yielding responses through changes in applied loading rates and strain-rate sensitivity exponents.

I. INTRODUCTION

The understanding and classification of complex patterns that emerge in science and engineering are a key component of technological developments across fields, introducing dimensional reduction of tools and paradigms that perform at multiple scales. The basic constituent of such a classification is a pattern characterization parameter that should be directly introduced from input data through simple computational steps. In the context of materials informatics for mechanical deformation applications, a major goal is the information hidden in total-strain maps, readily measured through digital image correlation (DIC) [1]. In crystal plasticity, information extracted from DIC has been focused on plastic slip accumulation in particular crystallographic directions, assisted by intense finite-element modeling [2–4]. However, the information is dependent on phenomenological constitutive laws that are changing with temperature and loading rate, especially under extreme conditions. In this paper, we introduce two functional tools based on principal component analysis and discrete wavelet transforms that aim to capture the onset of crystal plasticity through the analysis of total-strain fluctuations during mechanical loading. As a test case, we use these tools on DIC of polycrystalline samples, synthetically produced in a phenomenological crystal plasticity model for pure Al.

The application of modern statistical methods to identify transitions between phases with well-defined order parameters in materials has become quite common [5]. The recent theme in the physics and engineering communities is the application of machine learning methods so that the identification of a precise characterization parameter is avoided and automatic detection is achieved [6–13]. However, the absence of detailed knowledge may lead to overfitting artifacts and unsuccessful machine learning training. In this context, the use of unsupervised machine learning through principal component analysis (PCA) has been insightful [8,9,14–16].

The investigation of total strains typically prohibits the identification of structural defects, such as dislocations in crystalline solids and structural hot spots in amorphous solids, since a separation of elastic and plastic contributions to the strain is required if defects carry plastic flow [17]. In fact, standard mechanical testing does precisely that kind of a separation by plotting an elastic contribution (stress) as a function of the total contribution (total strain) (for strains $<5\%$). The onset of plasticity has always been connected to the daunting task of separation between elastic and plastic contributions that requires either standard mechanical testing or nondestructive testing through nanoindentation and defect imaging [18]. However, the determination of yield stress depends on environmental conditions, and there are still open questions in both simulations and experiments, especially in the context of amorphous solids [19–26].

DIC is an essential tool for acquiring full-field surface displacements towards strain maps of material surfaces at various resolutions, from millimeter to nanometer [27]. Through modern cameras and fast computational analysis, one may track displacements of distinct features in deformed samples. Nevertheless, DIC tracks only total displacements, and thus, its usefulness has mainly been the assessment of strain heterogeneity [28] or an inverse solution through validation of microstructurally accurate finite-element modeling [29]. Indeed, DIC has been useful for finding similarities in finite-element models of various types [1,29], with advanced multiscale models of microstructural deformation behavior [30–32], and machine learning models [33–35]. But the evolution of DIC total-strain profiles has led to rich information content that may be adequate to infer material properties related to yielding, hardening, and eigenstrains. Here, we explore the usefulness of this information by using strain maps to extract the yield point of a polycrystalline microstructure through PCA or discrete wavelet transforms (DWTs).
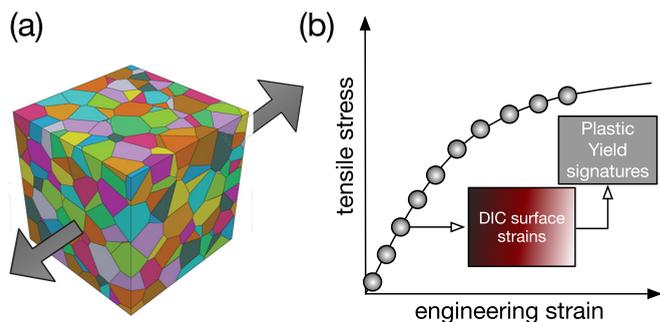
FIG. 1. Schematic of the main scenario investigated in this work. A polycrystalline sample with an unknown mechanical response is being (a) uniaxially loaded under tension and (b) imaged on one of the surfaces through digital image correlation (DIC). The total-strain image output of DIC serves as the basis of an inquiry on yielding signatures in DIC correlations as more images are collected. In this work, we utilize two tools based on principal component analysis and discrete wavelet transforms. We consider various yield behaviors in this work by phenomenologically controlling the loading rate and rate hardening exponent ($\dot{\gamma}, n$).

In this paper, we focus on polycrystalline metals and small quasielastic strains ($<0.3\%$) and the incipient transition to plasticity. Our focus is on the development of tools that can reliably extract key material properties directly out of total-strain maps and fill two needs at once: perform efficient dimensional reduction of DIC image sequences and also identify key material properties without the use of local or global stress information. For this purpose, we perform simulations in quasi-two-dimensional (quasi-2D) and three-dimensional (3D) samples by using a phenomenological crystal plasticity model that incorporates well-established polycrystalline deformation mechanisms [36].

In the context of this model, the PCA analysis of strain fluctuations can be used to accurately identify yield points. If we vary the microstructural hardening exponent and strain rate, the plasticity transition is qualitatively modified, but the developed measures still efficiently track the yield point. Furthermore, we demonstrate that DWT coefficients, designed to identify localized features in images, can be used to identify the onset of plasticity at the material yield point. We conclude by comparing the two complementary approaches and discuss how to generalize them to learning additional properties, such as hardening and damage parameters, as well as to mutually distinguish various hardening and damage mechanisms.

II. METHODS

We consider synthetic data of uniaxial tensile mechanical deformation in a polycrystalline sample, where the physics of crystal plasticity is captured in the most common, recognizable way. The model is uniaxially loaded along the x direction, and x-y surface images were produced for close-by strain intervals up to, typically, 0.3% total strain, where all samples have already yielded. The focus of this work is the analysis of these image sequences in a way that key information about the yielding transition is directly extracted from total-strain evolution (see also Fig. 1). We utilize phenomeno-

logical crystal plasticity in the continuum [37] to solve for material deformation due to elasticity, plasticity, and damage evolution within the sample.

Regarding the plasticity model, we consider [36–38] the case of tensile loading in the x direction for 2D and 3D specimens which are periodic in all directions and have sample dimensions in (x, y, z) of (512,512,2) and (64,64,64), respectively, where each cell can be interpreted as a representative volume element with dimensions of 2 μm in each direction, promoting the perspective of investigating 1 mm² 2D or submillimeter 3D samples. We study two different geometries so that the geometry effect on our measures is checked. The crystalline structure of the material is fcc Al, with standard stiffness coefficients $C_{11} = 106.75$ GPa, $C_{12} = 60.41$ GPa, and $C_{44} = 28.34$ GPa (in reference to the cubic coordinates). The importance of the examples studied is that the simulated dimensions can be achieved by common DIC procedures [1].

Details of the model's hardening dynamics can also be found in Refs. [36,38]. The model is built upon typical phenomenological crystal plasticity assumptions, capturing the essential aspects of slip-based macroscale plasticity through a combination of fundamental assumptions and basic constitutive laws that have been confirmed in various metals [37]. In this work, modeling examples cannot be accurate in capturing delicate plasticity features that relate to defect-driven latent hardening or non-Schmid effects [39]; they still capture in a self-consistent manner the basic physical mechanisms involved in the transition from elasticity to plasticity as it takes place in most metals. In summary, the model captures finite deformations in a cubic grid, used to calculate constitutively plastic distortion rates along all 12 fcc slip systems. All samples have 256 grains that are distributed randomly using a Voronoi tesselation [40] [see also Fig. 2(a)], and the model is solved by using a spectral approach [38]. To estimate the plastic deformation tensor and its rate, we iteratively solve

$$\dot{F}_p = L_p F_p, \tag{1}$$

where $L_p = \sum_\alpha \dot{\gamma}^\alpha s^\alpha \otimes n^\alpha$, with s and n being the unit vectors along the slip direction and slip plane normal, respectively, and α being the index of a slip system. The total deformation tensor is commonly split into elastic and plastic parts through $F = F^e F^p$. We consider all 12 fcc slip systems which may become active in our single crystal with fixed crystalline orientation. The slip rate $\dot{\gamma}^\alpha$ is given by the basic phenomenological crystal plasticity constitutive equation [37,41]

$$\dot{\gamma}_\alpha = \dot{\gamma}_0 \left| \frac{\tau^\alpha}{g^\alpha} \right|^n \mathrm{sgn}(\tau^\alpha), \tag{2}$$

where $\dot{\gamma}_0 = 0.001/s$ is the reference shear rate; $\tau^\alpha = S \cdot (s^\alpha \otimes n^\alpha)$ is the resolved shear stress at slip resistance g^α, with $S = [C]E^\epsilon$ being the Second Piola-Kirchoff stress tensor and n taking the values (5,10) in this work (the inverse of the strain rate sensitivity exponent $m = 1/n$); and g^α is the slip resistance for a slip system α. Hardening is provided by another saturation-type crystal plasticity constitutive law [42]:

$$\dot{g}^\alpha = \sum_{\beta=1}^{12} h_{\alpha\beta} |\dot{\gamma}^\beta|, \tag{3}$$
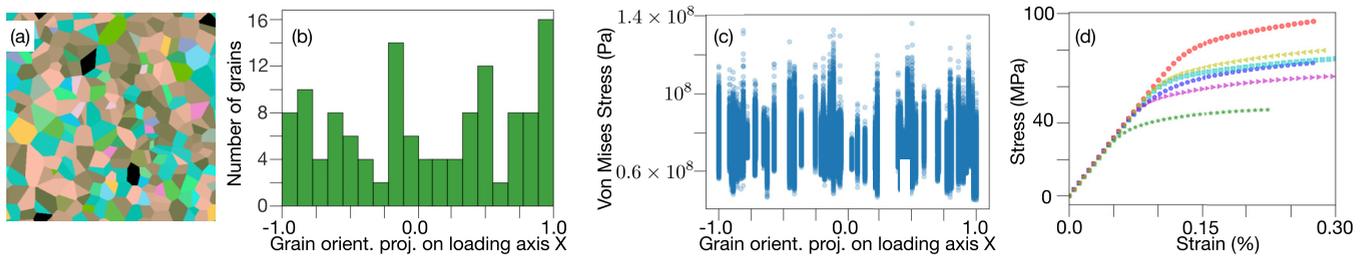
FIG. 2. Polycrystalline texture and mechanical response. (a) Polycrystalline texture of samples studied in this work on $512 \times 512 \times 2$ 2D and $64 \times 64 \times 64$ (3D) grids, with 256 grains in each microstructure. (b) Grain orientation distribution through loading-axis projection (given the representation through Bunge-Euler angles with respect to the x-axis projection is $\cos\phi_1\cos\phi_2$-$\sin\phi_1\sin\phi_2\cos\Phi$). (c) Von Mises stress values on the microstructure of the case $(\dot{\gamma}, n) = \{5 \times 10^{-2}/\text{s}, 10\}$ for the 2D grid at total strain of 0.25%. (d) The mechanical response (average stress along the loading x direction vs loading strain) for all studied samples, with loading along the y direction with various loading rates and rate sensitivity exponents $(\dot{\gamma}, n)$ in the 2D cases ($\varhexagon$: $\{5 \times 10^{-4}/\text{s}, 5\}$, $\star$: $\{5 \times 10^{-4}/\text{s}, 10\}$, $\bullet$: $\{5 \times 10^{-3}/\text{s}, 5\}$, $\triangleright$: $\{5 \times 10^{-3}/\text{s}, 10\}$, $\triangleleft$: $\{5 \times 10^{-4}/\text{s}, 10\}$) and also the 3D case ($\square$: $\{5 \times 10^{-4}/\text{s}, 10\}$). The 3D sample has loading and strain-rate sensitivity identical to those in the 2D case with parameters $\{5 \times 10^{-4}/\text{s}, 10\}$.

where $h_{\alpha\beta}$ is the hardening matrix,

$$h_{\alpha\beta} = q_{\alpha\beta}h_0\left[\text{sgn}\left(1 - \frac{g^\beta}{g^\beta_\infty}\right)\left|1 - \frac{g^\beta}{g^\beta_\infty}\right|^p\right], \qquad (4)$$

which phenomenologically captures the micromechanical interactions between different slip systems. Here, $h_0 = 75$ MPa and $p = 2.25$ are slip hardening parameters that are typically assumed to be identical for all fcc systems owing to the underlying dislocation reactions. g^β is the resistance to shear on the β slip system, and g^β_∞ is the saturated shear resistance on slip system β (set at $g^s = 63$ MPa for all slip systems); the shear resistances asymptotically evolve towards saturation. The parameter $q_{\alpha\beta}$ is a measure for latent hardening, and its value is taken as 1.0 for mutually coplanar slip systems and 1.4 otherwise, rendering the hardening model anisotropic. It is common in the literature to find several variants of the above constitutive laws; nevertheless, we believe that the results in this work are relatively model independent.

A known way to control and modify the yield stress in this model is through the change in the rate sensitivity exponent $m = 1/n$. A change in the value of n naturally occurs through changes in conditions (e.g., temperature). Here, we modify the exponent n by considering the values 5 and 10 while the strain rate is modified through 3 orders of magnitude (5×10^{-4}, 5×10^{-3}, and 5×10^{-2}). As Fig. 2(d) clearly shows, the yield stress changes by a factor of 2, and the hardening exponent increases drastically as well. Also, each point in Fig. 2(d) implies a corresponding image of total strain that is directly captured during the simulation, emulating the DIC procedure [33,34]. Stress and strain profiles generated in our simulations [Figs. 3(a)–3(i)] can be readily compared to profiles generated by DIC techniques for polycrystalline metals at small, quasielastic applied loads [1].

III. RESULTS

A typical first impression after observing the system behavior is that the von Mises stress fluctuations across a particular sample [seen in Fig. 2(c)] do not display any particular orientation preference across the polycrystalline sample in the case $(\dot{\gamma}, n) = \{5 \times 10^{-2}/\text{s}, 10\}$ at a total strain of 0.25%. Also,

patterning in images like the ones in Fig. 3 commonly appears mundane: There appears to be no clear correlation of the impact that yielding has on the total strain since the plastic distortion F_p becomes relatively important. The principal reasons for this mundane impression are, clearly, the presence of an always finite, superposing, plasticity-dependent elastic contribution and the fact that plasticity is not homogeneous in the sample, with only a few locations at high values, pointing to the fundamentally important plastic localization physics [37]. These findings are consistent with the accumulated understanding in materials science that grain-boundary misorientations correspond more to emerging stresses and plastic distortions than actual grain orientations. Nevertheless, to this day, classification of misorientations in polycrystals represents a daunting classification challenge, where there is a space of five dimensions misorientation dimensions on a grain boundary [43]. In this paper, we focus on two tools for generating measures that naturally, and fundamentally, relate to the onset of plasticity. At the possible expense of computational complexity, we introduce two total-strain measures that are sensitive to the onset of plasticity: one from a PCA transform analysis of the total-strain images, designed to capture total-strain fluctuations, and one from a DWT analysis, designed to capture the onset of strain localization.

Principal component analysis serves the change in basis in N data vectors E_k (here capturing the norm $|F - I|$ of total distortion across the sample), each entry of which captures spatial locations of total number V, so that predominant correlations are detected in a few principal directions. In this case, each E_k is a flattened total-strain vector of $N = L_x * L_y$, corresponding to an $L_x \times L_y$ total-strain image [see Figs. 1, 3(c), 3(f) and 3(i)]. The success of the method is gauged by the capacity to capture, almost completely ($>98\%$), the relative fluctuations in just two to three principal vectors, like the one shown in Fig. 4(a) or the ones shown in Figs. 4(b), 4(c), 5(b), and 5(c) for our case. In this application, as can be seen in Figs. 4(d), PCA works well. Each component [e.g., Fig. 4(a)] represents a "characteristic" fluctuation pattern in the evolution of data vectors.

Then, these vectors can be projected back to the original data vectors through a vector dot product, so that overlap with
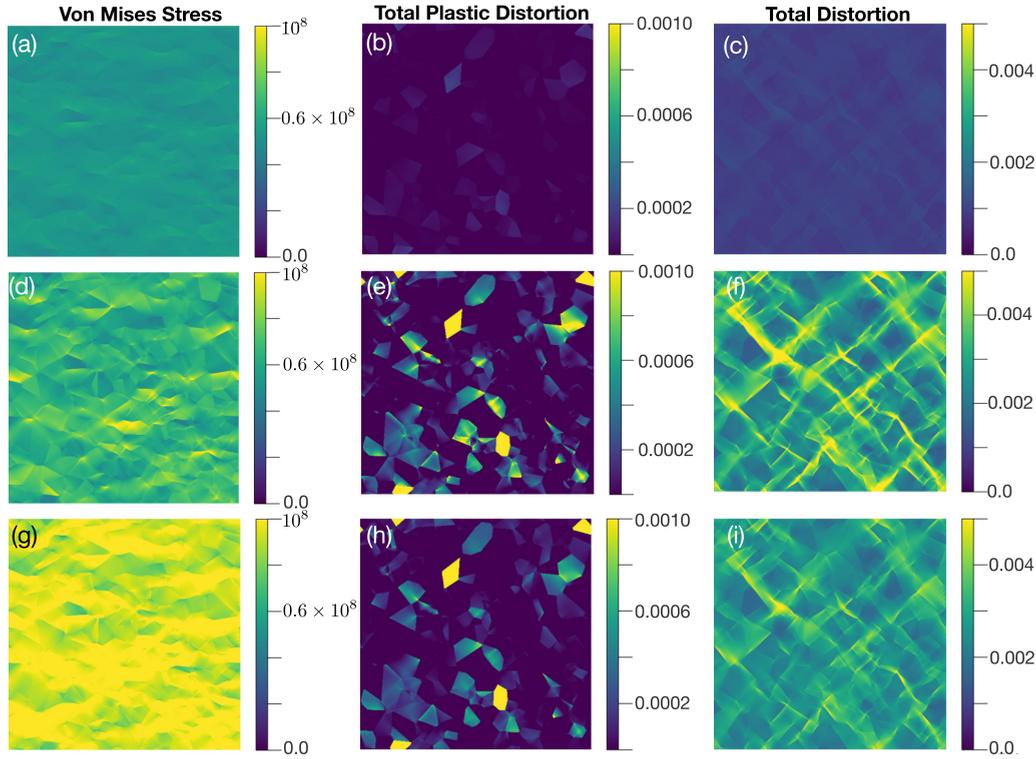
FIG. 3. Von Mises stress and plastic and total distortion at the yield point and postyield strain. (a), (d), and (g) Von Mises stress, (b), (e), and (h) plastic distortion, defined as $|F_p - I|$, and (c), (f), and (i) total distortion, defined as $|F - I|$. (a)–(c) At the yield point (0.12% total strain) for 2D samples and loading rate and rate sensitivity exponent $(\dot{\gamma}, n) = \{5 \times 10^{-4}/\text{s}, 10\}$, (d)–(f) at 0.25% total strain for loading rate and rate sensitivity exponent $(\dot{\gamma}, n) = \{5 \times 10^{-4}/\text{s}, 10\}$, and (g)–(i) at 0.25% total strain for loading rate and rate sensitivity exponent $\{5 \times 10^{-2}/\text{s}, 10\}$.

data vectors is tracked. For the data vectors' fluctuations to be directly comparable, each data vector has to have the same average value (0) and standard deviation (1), so data vectors are rescaled in a standard way:

$$\tilde{E}_k = \frac{E_k - \langle E_k \rangle}{\sqrt{\langle E_k^2 \rangle - \langle E_k \rangle^2}}, \qquad (5)$$

where the $\langle \cdot \rangle$ implies a spatial average $\langle E_k \rangle = \sum_i E_k^{(i)}$, with i counting spatial locations.

Principal components emerge through the singular-value decomposition of the matrix $X = \{E_k\}$ for $k \in$ {range where data are collected}, including N lines and V columns and then focusing on the top singular values and components. In other words, the rectangular $N \times V$ matrix X is decomposed to

$$X = U \Sigma W^T, \qquad (6)$$

where U is an $N \times N$ matrix containing columns that are orthogonal unit vectors of length N that are known as "left singular vectors" of X. Also, W is a $V \times V$ matrix whose columns are also orthogonal unit vectors of length V and are known as the right singular vectors of X. For every singular vector s_i, there is a corresponding singular value σ_i.

The condition of capturing most fluctuations in the system is equivalent to identifying the eigenvalues σ of the covariance matrix of the data vectors $C = X^T X / (n - 1)$, which represent the variance of the fluctuations, and then the top three eigenvalues should roughly equal 99%. It is easy to show that $C =$

$V[\Sigma^2/(n - 1)]V^{-1}$, which promotes the equivalence of singular values with $\sqrt{\lambda(n - 1)}$. Plotting the sum of σ with more principal components leads to the conclusion [see Fig. 4(d)] that keeping only two components completely captures the total data variance across loading it. In retrospect, this is an outcome of the fact that plasticity is controlled principally by two distinct states: the elastic one before yielding and the plastic one.

Given that the singular values are labeled σ_i for the ith component, the projection (dot product) of a component s_i on one of the data vectors $\tilde{E}_k$ is defined here as

$$P_{(i)}^{(k)} = \frac{s_i \cdot E_k}{\sqrt{\sigma_i}}. \qquad (7)$$

As seen in Fig. 4(e), where $P_1^{(k)}$ and $P_2^{(k)}$ are plotted against each other, the maximum coincides with the sample's yield point, identified from stress-strain curves. By plotting the projections with respect to the applied strain, it becomes clear that the first component projection is decreased at yielding, while the second has a fluctuation-driven behavior, peaking at the plasticity transition [see also Fig. 4(f)]. In addition, the yield strain e_y can be defined as the finite extremum of the second derivative of stress with respect to the strain, after fitting it with a continuous third-order polynomial. In this way, we can compare the two definitions, shown in Fig. 4(h). So instead of
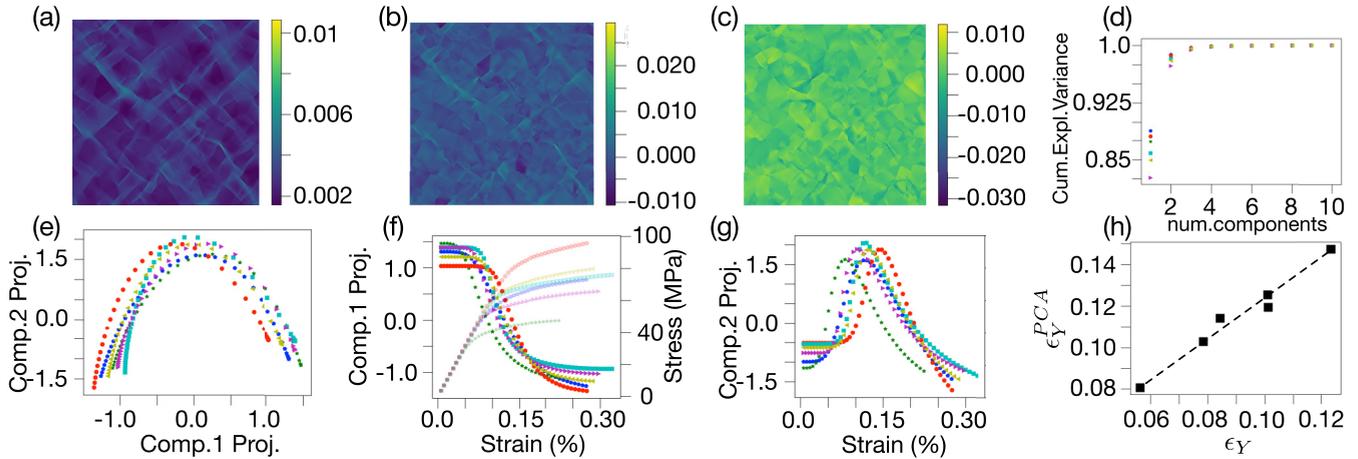
FIG. 4. PCA of total strain profiles and order parameters for plasticity. Principal component analysis is applied on properly normalized total-strain ($|F - I|$) maps. (a) Total-strain map for strain 0.25% and $(\dot{\gamma}, n) = : \{5 \times 10^{-3}/s, 10\}$, similar to the cases shown in Figs. 3(c), 5(f) and 3(i), for examples, after subtracting the mean, taking the absolute value, and then dividing by the sample strain variance. (b) First and (c) second PCA components for $(\dot{\gamma}, n) = \{5 \times 10^{-4}/s, 10\}$. (d) Principal component cumulative variance of the components, showing a saturation to more than 95% of the observed variability by just utilizing two components. (e) The projection of the first ($P_1^{(k)}$) and second ($P_2^{(k)}$) components on the strain map samples after normalizing with $\sqrt{\sigma_i}$, where σ_i is the corresponding singular case, for the various material cases discussed in Fig. 2, with symbols corresponding to the following $(\dot{\gamma}, n)$: $\bigcirc$, $\{5 \times 10^{-4}/s, 5\}$; $\star$, $\{5 \times 10^{-4}/s, 10\}$; $\bullet$, $\{5 \times 10^{-3}/s, 5\}$; $\triangleright$, $\{5 \times 10^{-3}/s, 10\}$; and $\triangleleft$, $\{5 \times 10^{-4}/s, 10\}$ in the 2D cases and $\square$, $\{5 \times 10^{-4}/s, 10\}$ in the 3D case. The 3D sample has loading and strain-rate sensitivity identical to those in the 2D case, $\{5 \times 10^{-4}/s, 10\}$. (f) The first component projection $P_1^{(k)}$ and, in the background, the stress-strain curves from Fig. 2. A clear correlation with stress-strain behavior is seen in the peak of the second PCA component and the decrease of the first PCA component, signifying the onset of the elastic-plastic transition. (g) The second component projection $P_2^{(k)}$, defined in text, as a function of the applied strain. (h) The PCA-predicted yield point vs the actual yield point (found from the stress-strain curve).

using an engineering definition of yield stress, we suggest that the yield strength of any sample is uniquely defined as

$$\epsilon_y|_{\text{PCA}} = \epsilon_y \left\{ \frac{dP_2^{(k)}}{d\epsilon_k} = 0 \right\}, \qquad (8)$$

$$\sigma_y|_{\text{PCA}} = C\epsilon_y. \qquad (9)$$

The use of PCA analysis is focused on understanding *fluctuations* present in images of total strain. However, another possibility emerges through the investigation of total-strain local features. This endeavor can be achieved through using a DWT that is designed to capture localized features in any image. In our case, we consider the image where the x direction

signifies "space," while the y direction signifies applied-load evolution.

The DWT, as formulated by Daubechies [44], has been extensively used to decompose time series fluctuations. In contrast to Fourier transforms, which decompose fluctuations across a Fourier frequency continuum, the wavelet decomposition is performed across a discrete set of scales, and the component amplitude measures how much variability exists between adjacently located averages associated with a particular scale. Examples of the wavelet decomposition's usefulness are abundant in science and engineering and, for example, include sleep state patterns [45] and stochastic fluctuations in binary stars [46].

Regarding wavelets, they are real functions of real numbers, each of which is derived from the mother using translation and scaling: $\Psi_{s,x}(t) = 2^{s/2}\Psi(2^s t + x)$, where s, x are real numbers, Ψ is the mother wavelet, and $\Psi_{s,x}$ is a wavelet of scale s and translation x; in other words,

$$\Psi^{s,x}(t) = \frac{1}{\sqrt{|s|}} \psi\left(\frac{t-x}{s}\right) \qquad (10)$$

FIG. 5. PCA for surfaces of 3D samples. A $64 \times 64 \times 64$ simulation was performed at $(\dot{\gamma}, n) = : \{5 \times 10^{-4}/s, 10\}$, and the same process as in Fig. 4 leads to analogous results. (a) Grain structure in a simulated sample with 256 grains. Each color corresponds to the grain orientation's Bunge Euler angles with respect to the projection on the x axis. (b) First PCA component, analogous to the one in Fig. 4. (c) Second PCA component, analogous to the one in Fig. 4. A comparison of the components' overlap in two and three dimensions shows good agreement, with no qualitative differences (see also Fig. 4).

for $s \neq 0$, with $\langle \Psi \rangle = 0$. In this work, we use the Daubechies wavelet transform, which uses the basic DWT structure, where any square, real, integrable function $[y(t) \in L^2\{R\}]$ can be expressed in terms of the transform at multiple scales:

$$y(t) = \sum_m \sum_n \tilde{y}_{m,n} 2^{-m/2} \tilde{\psi}(2^{-m}t - n) \qquad (11)$$
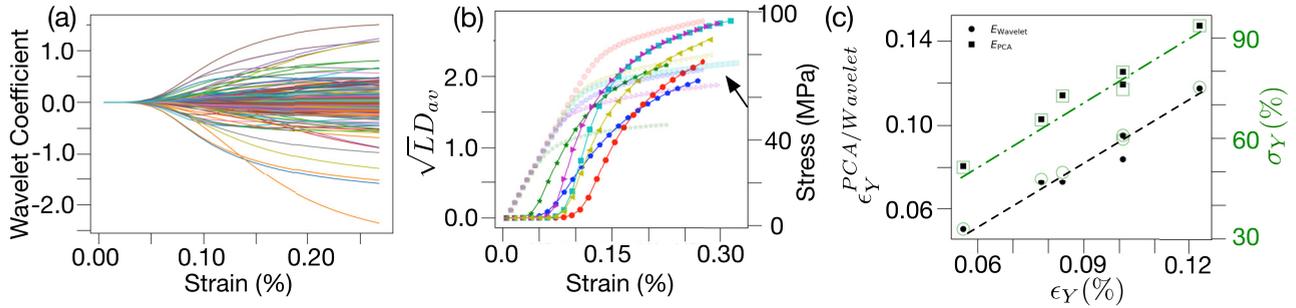
FIG. 6. Wavelet coefficients and the onset of yielding. (a) A subset of the Daubechies coefficients in the strain direction as a function of the applied strain for the case $(\dot{\gamma}, n) = : \{5 \times 10^{-4}/s, 10\}$. (b) Average (spatially) wavelet coefficients as a function of strain for all cases with symbols analogous to those in the other figures for the following $(\dot{\gamma}, n)$: $\bigcirc$, $\{5 \times 10^{-4}/s, 5\}$; $\star$, $\{5 \times 10^{-4}/s, 10\}$; $\bullet$, $\{5 \times 10^{-3}/s, 5\}$; $\triangleright$, $\{5 \times 10^{-3}/s, 10\}$; and $\triangleleft$, $\{5 \times 10^{-4}/s, 10\}$ in the 2D cases and $\square$, $\{5 \times 10^{-4}/s, 10\}$ in the 3D case. The average onset of the Daubechies coefficients coincides with the yield point ϵ_y, detected through measuring applied loads. (c) $\epsilon_Y^{\text{Wavelet}}$ is defined through the point of the first nonzero value in (b). A natural comparison between PCA and wavelet predictions is shown for both the yield strain ϵ_Y and yield stress σ_Y, where the projected yield stress is just the yield strain multiplied by the elastic modulus. Lines are a guide to the eye.

and

$$\tilde{y}_{m,n} = \int_{-\infty}^{\infty} 2^{-m/2} \psi(2^{-m}t - n)y(t)dt, \quad (12)$$

where the functions ψ and $\bar{\psi}$ are the wavelet basis functions for analysis and synthesis [44] and they are biorthogonal $[\langle \psi(t)\bar{\psi}(t-m)\rangle = \delta_{m,0}$ and $\langle \psi(t)\bar{\psi}(t-m)\rangle = \delta_{m,0}]$. Towards the generalization of this construction in two dimensions, the 2D wavelet transform of an image $f(x)$ computes the set of inner products

$$d_j^k[n] = \langle f, \psi_{j,n}^k \rangle \quad (13)$$

for scales $j \in Z$, position $n \in Z^2$, and orientation $k \in \{H, V, D\}$.

The wavelet atoms are defined by scaling and translating three mother atoms $\{\psi^H, \psi^V, \psi^D\}$:

$$\psi_{j,n}^k(x) = \frac{1}{2^j}\psi^k\left(\frac{x - 2^j n}{2^j}\right). \quad (14)$$

The scaling function and directional wavelets are composed of the product of a one-dimensional scaling function ϕ and corresponding wavelet ψ which follow

$$\phi(x, y) = \phi(x)\phi(y), \quad (15)$$

$$\psi^H(x, y) = \psi(x)\phi(y), \quad (16)$$

$$\psi^V(x, y) = \phi(y)\psi(x), \quad (17)$$

$$\psi^D(x, y) = \psi(x)\psi(y). \quad (18)$$

A high number of vanishing moments allows us to better compress regular parts of the signal. However, increasing the number of vanishing moments also increases the size of the support of the wavelets, which can be problematic in the part where the signal is singular (for instance, discontinuous). In this work, we focus on the properties of ψ^V and thus d_2^D.

Here, our 2D images are composed of total-strain features in columns, while each row contains a different applied strain. For clarity, in this way, the images have 30 rows but 2^{18} or 2^{16} columns. We focus solely on the features of ψ^V which

capture localization along the loading direction. By plotting DWT coefficients (just a small sample of 500 coefficients out of the 2^{18} or 2^{16}) along the loading direction (see Fig. 6), for a particular yielding case, one can see that the coefficients become nonzero only at a particular value, which can be associated with the yield point. By performing a spatial average of all coefficients' absolute values, one can calculate

$$D_{av} = \frac{1}{N}\sum_{n \in [1,N]} d_2^D[n], \quad (19)$$

where N is the number of pixels and the behavior of D_{av} is shown across all cases in Fig. 6(b), with coefficients acquiring nonzero values at a point that resembles the yielding transition very much. So in this way, we suggest that another computational definition of the yield point is

$$e_y|_{\text{Wavelet}} = \text{LOC}\{\max(D_{av} = 0)\}, \quad (20)$$

$$\sigma_y|_{\text{Wavelet}} = C * e_y. \quad (21)$$

IV. DISCUSSION

The PCA and wavelet yield point definitions can also be compared directly, as shown in Fig. 6(c). As the direct comparison shows, the predictions from the two methods are closely related, possibly giving an edge to wavelets if the focus is on the identification of the departure from elasticity, while the predictive edge belongs to PCA when elastoplastic fluctuations become maximum and elastic deformation disappears.

It is worth noticing that it was expected that the PCA predictions are always larger in magnitude than the wavelet ones. The reason is that the wavelet-based criterion concentrates on detecting the onset of localized fluctuations, while the PCA-based one focuses on detecting the maximum of the fluctuations (not localization). Nevertheless, the evidently constant offset between wavelet and PCA predictions seems to be accidental due to the fact that elastic-plastic nonlinearities in the models considered are quantitatively similar. A possible consideration of highly nonlinear elastic responses and

unconventional hardening should have a strong effect on the offset between wavelet and PCA predictions.

In conclusion, we presented two distinct computational tools that are easily implemented through modern computational software and can be used towards the identification of yielding in polycrystals through only total-strain measurements, without the need to separate elastic from plastic contributions from total-strain profiles. In the performed simulations, each pixel's linear dimension corresponds to 2 μm, and the linear size of tracked areas approaches 1 mm. Thus, standard experimental tests should be capable of matching these conditions. By comparing two distinct geometries, we found that the transition from elasticity to plasticity is equally detectable in 2D and 3D cases. The effects reported here originate in the large-scale features of elastic fluctuations during the transition from elasticity to plasticity, without explicit connection to the character and dynamics of plasticity defects, such as dislocation dynamics and slip localization. The studied models are coarse grained and do not capture the detailed mechanisms of plastic slip localization. Atomic resolution in DIC would introduce additional features to the behavior of PCA/DWT observables, with expected resolution-dependent scaling phenomena, in a manner analogous to the common collective dynamical transition of complex physical systems [47]. Then, the identified PCA/DWT behavior would be enriched with additional physical features and finite-size scaling (originating from the increasing resolution) that may unveil additional nanoscale physical mechanisms. While beyond this work's scope, it is important to explore the application of these methods to discrete dislocation plasticity models [48] in connection with previously identified collective plasticity mechanisms [49,50], so that localization criteria become associated with the behavior of PCA/DWT observables.

In addition, large-scale elastic fluctuations are influenced by plastic yielding and may also unveil hardening and damage sample behaviors beyond the yield point. Characteristically, one may tentatively conclude through data like those in Fig. 4(g) that the slope of $P_2^{(k)}$ beyond yielding is inversely related to the hardening coefficient. Through preliminary studies, we find analogous dependencies for damaged specimens' synthetic data. The generality of these dependencies and the formulations towards microscopically motivated scaling functions [51] will be the subject of future works. In addition, it is worth exploring experimental validation routes and ways to identify further material properties by detailed analysis of total-strain fluctuations in evolving images.

ACKNOWLEDGMENTS

[1] H. Schreier, J.-J. Orteu, and M. A. Sutton, *Image Correlation for Shape, Motion and Deformation Measurements: Basic Concepts, Theory and Applications* (Springer US, New York, NY, 2009), Vol. 1.

[2] A. Guery, F. Hild, F. Latourte, and S. Roux, Identification of crystal plasticity parameters using DIC measurements and weighted FEMU, Mech. Mater. **100**, 55 (2016).

[3] N. Grilli, P. Earp, A. C. Cocks, J. Marrow, and E. Tarleton, Characterization of slip and twin activity using digital image correlation and crystal plasticity finite element simulation: Application to orthorhombic α-uranium, J. Mech. Phys. Solids **135**, 103800 (2020).

[4] A. Githens, S. Ganesan, Z. Chen, J. Allison, V. Sundararaghavan, and S. Daly, Characterizing microscale deformation mechanisms and macroscopic tensile properties of a high strength magnesium rare-earth alloy: A combined experimental and crystal plasticity approach, Acta Mater. **186**, 77 (2020).

[5] P. W. Anderson, *Basic Notions of Condensed Matter Physics* (Benjamin-Cummings, Menlo Park, CA, 1984).

[6] G. Carleo, I. Cirac, K. Cranmer, L. Daudet, M. Schuld, N. Tishby, L. Vogt-Maranto, and L. Zdeborov, Machine learning and the physical sciences, Rev. Mod. Phys. **91**, 045002 (2019).

[7] E. P. Van Nieuwenburg, Y. H. Liu, and S. D. Huber, Learning phase transitions by confusion, Nat. Phys. **13**, 435 (2017).

[8] W. Hu, R. R. Singh, and R. T. Scalettar, Discovering phases, phase transitions, and crossovers through unsupervised machine learning: A critical examination, Phys. Rev. E **95**, 062122 (2017).

[9] S. J. Wetzel, Unsupervised learning of phase transitions: From principal component analysis to variational autoencoders, Phys. Rev. E **96**, 022140 (2017).

[10] B. S. Rem, N. Kming, M. Tarnowski, L. Asteria, N. Flschner, C. Becker, K. Sengstock, and C. Weitenberg, Identifying quantum phase transitions using artificial neural networks on experimental data, Nat. Phys. **15**, 917 (2019).

[11] C. Giannetti, B. Lucini, and D. Vadacchino, Machine learning as a universal tool for quantitative investigations of phase transitions, Nucl. Phys. B **944**, 114639 (2019).

[12] W. Zhang, J. Liu, and T. C. Wei, Machine learning of phase transitions in the percolation and *XY* models, Phys. Rev. E **99**, 032142 (2019).

[13] Q. Ni, M. Tang, Y. Liu, and Y. C. Lai, Machine learning dynamical phase transitions in complex networks, Phys. Rev. E **100**, 052312 (2019).

[14] L. Wang, Discovering phase transitions with unsupervised learning, Phys. Rev. B **94**, 195105 (2016).

[15] C. Wang and H. Zhai, Machine learning of frustrated classical spin models. I. Principal component analysis, Phys. Rev. B **96**, 144432 (2017).

[16] C. Ruscher and J. Rottler, Correlations in the shear flow of athermal amorphous solids: A principal component analysis, J. Stat. Mech. (2019) 093303.

[17] D. Richard, M. Ozawa, S. Patinet, E. Stanifer, B. Shang, S. A. Ridout, B. Xu, G. Zhang, P. K. Morse, J. L. Barrat, and L. Berthier, Predicting plasticity in disordered solids from structural indicators, Phys. Rev. Mater. **4**, 113609 (2020).

[18] S. Pantelakis, E. P. Koumoulos, C. A. Charitidis, N. M. Daniolos, and D. I. Pantelis, Determination of onset of plasticity (yielding) and comparison of local mechanical properties of friction stir welded aluminum alloys using the micro and nanoindentation techniques, Int. J. Struct. Integr. **4**, 143 (2013).

[19] E. D. Cubuk, S. S. Schoenholz, J. M. Rieser, B. D. Malone, J. Rottler, D. J. Durian, E. Kaxiras, and A. J. Liu, Identifying Structural Flow Defects in Disordered Solids Using Machine-Learning Methods, Phys. Rev. Lett. **114**, 108001 (2015).

[20] S. S. Schoenholz, E. D. Cubuk, D. M. Sussman, E. Kaxiras, and A. J. Liu, A structural approach to relaxation in glassy liquids, Nat. Phys. **12**, 469 (2016).

[21] V. Bapst, T. Keck, A. Grabska-Barwiska, C. Donner, E. D. Cubuk, S. Schoenholz, A. Obika, A. Nelson, T. Back, D. Hassabis, and P. Kohli, Unveiling the predictive power of static structure in glassy systems, Nat. Phys. **16**, 448 (2020).

[22] P. Ronhovde, S. Chakrabarty, D. Hu, M. Sahu, K. Sahu, K. Kelton, N. Mauro, and Z. Nussinov, Detecting hidden spatial and spatio-temporal structures in glasses and complex physical systems by multiresolution network clustering, Eur. Phys. J. E **34**, 105 (2011).

[23] E. Boattini, M. Dijkstra, and L. Filion, Unsupervised learning for local structure detection in colloidal systems, J. Chem. Phys. **151**, 154901 (2019).

[24] E. Boattini, S. Marn-Aguilar, S. Mitra, G. Foffi, F. Smallenburg, and L. Filion, Autonomously revealing hidden local structures in supercooled liquids, Nat. Commun. **11**, 5479 (2020).

[25] S. Patinet, D. Vandembroucq, and M. L. Falk, Connecting Local Yield Stresses with Plastic Activity in Amorphous Solids, Phys. Rev. Lett. **117**, 045501 (2016).

[26] S. Patinet, A. Barbot, M. Lerbinger, D. Vandembroucq, and A. Lematre, Origin of the Bauschinger Effect in Amorphous Solids, Phys. Rev. Lett. **124**, 205503 (2020).

[27] M. A. Sutton and F. Hild, Recent advances and perspectives in digital image correlation, Exp. Mech. **55**, 1 (2015).

[28] J. C. Stinville, W. C. Lenthe, M. P. Echlin, P. G. Callahan, D. Texier, and T. M. Pollock, Microstructural statistics for fatigue crack initiation in polycrystalline nickel-base superalloys, Int. J. Fract. **208**, 221 (2017).

[29] D. Lunt, R. Thomas, M. Roy, J. Duff, M. Atkinson, P. Frankel, M. Preuss, and J. Quinta da Fonseca, Comparison of sub-grain scale digital image correlation calculated using commercial and open-source software packages, Mater. Charact. **163**, 110271 (2020).

[30] T. Mäkinen, P. Karppinen, M. Ovaska, L. Laurson, and M. J. Alava, Propagating bands of plastic deformation in a metal alloy as critical avalanches, Sci. Adv. **6**, eabc7350 (2020).

[31] J. Koivisto, M.-J. Dalbe, M. J. Alava, and S. Santucci, Path (un)predictability of two interacting cracks in polycarbonate sheets using digital image correlation, Sci. Rep. **6**, 32278 (2016).

[32] T. Mäkinen, A. Miksic, M. Ovaska, and M. J. Alava, Avalanches in Wood Compression, Phys. Rev. Lett. **115**, 055501 (2015).

[33] Z. Yang, S. Papanikolaou, A. C. Reid, W. K. Liao, A. N. Choudhary, C. Campbell, and A. Agrawal, Learning to predict crystal plasticity at the nanoscale: Deep residual networks and size effects in uniaxial compression discrete dislocation simulations, Sci. Rep. **10**, 8262 (2020).

[34] S. Papanikolaou, M. Tzimas, A. C. Reid, and S. A. Langer, Spatial strain correlations, machine learning, and deformation history in crystal plasticity, Phys. Rev. E **99**, 053003 (2019).

[35] S. Papanikolaou, Microstructural inelastic fingerprints and data-rich predictions of plasticity and damage in solids, Comput. Mech. **66**, 141 (2020).

[36] F. Roters, M. Diehl, P. Shanthraj, P. Eisenlohr, C. Reuber, S. L. Wong, T. Maiti, A. Ebrahimi, T. Hochrainer, and H.-O. Fabritius, Comput. Mater. Sci. **158**, 420 (2019).

[37] R. Asaro and V. Lubarda, *Mechanics of Solids and Materials* (Cambridge University Press, Cambridge, 2006).

[38] S. Papanikolaou, P. Shanthraj, J. Thibault, C. Woodward, and F. Roters, Brittle to quasi-brittle transition and crack initiation precursors in crystals with structural inhomogeneities, Mater. Theory **3**, 5 (2019).

[39] A. Ma and F. Roters, A constitutive model for fcc single crystals based on dislocation densities and its application to uniaxial compression of aluminium single crystals, Acta Mater. **52**, 3603 (2004).

[40] W. H. Press, S. A. Teukolsky, W. T. Vetterling, and B. P. Flannery, *Numerical Recipes in C++: The Art of Scientific Computing* (Cambridge University Press, Cambridge, 1992).

[41] C. A. Bronkhorst, S. R. Kalidindi, and L. Anand, Polycrystalline plasticity and the evolution of crystallographic texture in FCC metals, Philos. Trans. R. Soc. London, Ser. A **341**, 443 (1992).

[42] S. B. Brown, K. H. Kim, and L. Anand, An internal variable constitutive model for hot working of metals, Int. J. Plast. **5**, 95 (1989).

[43] Y. S. Chen, W. Choi, S. Papanikolaou, and J. P. Sethna, Bending Crystals: Emergence of Fractal Dislocation Structures, Phys. Rev. Lett. **105**, 105501 (2010).

[44] I. Daubechies, Orthonormal bases of compactly supported wavelets, Commun. Pure Appl. Math. **41**, 909 (1988).

[45] C. Chiann and P. A. Morettin, A wavelet analysis for time series, Nonparametric Stat. **10**, 1 (1998).

[46] J. D. Scargle, T. Steiman-Cameron, K. Young, D. L. Donoho J. P. Crutchfield, and J. Imamura, The quasi-periodic oscillations and very low frequency noise of Scorpius X1 as transient chaos: A dripping handrail? Astron. J. **411**, L91 (1993).

[47] D. S. Fisher, Collective transport in random media: From superconductors to earthquakes, Phys. Rep. **301**, 113 (1998).

[48] L. P. Kubin, G. Canova, M. Condat, B. Devincre, Y. Pontikis, and V. Brechet, Dislocation microstructures and plastic flow: A 3D simulation, Solid State Phenom. **23**, 455 (1992).

[49] H. Song, D. Dimiduk, and S. Papanikolaou, Universality Class of Nanocrystal Plasticity: Localization and Self-Organization in Discrete Dislocation Dynamics, Phys. Rev. Lett. **122**, 178001 (2019).

[50] S. Papanikolaou and G. Po, Λ-Invariant and Topological Pathways to Influence the Strength of Submicron Crystals, Phys. Rev. Lett. **124**, 205502 (2020).

[51] S. Papanikolaou, Y. Cui, and N. Ghoniem, Avalanches and plastic flow in crystal plasticity: An overview, Modell. Simul. Mater. Sci. Eng. **26**, 013001 (2017).